Spreading of Disturbances in Realistic Models of Transmission Grids: Dependence on Topology, Inertia and Heterogeneity

Kosisochukwu P. Nnoli, *Graduate Student Member IEEE* and Stefan Kettemann

***Abstract*—The energy transition towards more renewable energy resources (RER) together with the reduction of conventional energy sources profoundly affects the frequency dynamics and electromechanical stability of electrical power networks. Here, we investigate the effect of different levels of grid inertia and its heterogeneous distribution on propagation patterns of disturbances in realistic models of power grids, including the Nigerian transmission network, the Ghana transmission network and the IEEE 118 bus test-grid as well as a Cayley-tree network, as a model grid without cycles, and the Square-grid power network as a strongly meshed model grid. These studies are conducted with the DigSILENT PowerFactory software and compared with results obtained from swing equations.**

Results show that the times of arrival of frequency deviations as function of geodesic distance from the contingency are more clustered and decay faster in more meshed grids than in tree-like or weakly meshed grids. In order to take into account the inhomogenous distribution of inertia, we define an effective distance r_{eff} and find it to be more strongly correlated with the arrival time than the geodesic distance. A ballistic equation for the arrival time, with a velocity derived from the swing equation, provides then a strict lower bound for all effective distances. The fitted velocity decays with a power law with grid inertia. Decreasing the magnitude of grid inertia by increasing the magnitude of RER is thereby found to increase the travel velocity of disturbances and reduce the time a disturbance needs to spread throughout the grid.

***Index Terms*—Grid disturbance spread, power grid topology, transient stability, linear response theory, frequency dynamics, heterogeneous inertia, effective distance.**

I. Introduction

THE inertia of the rotating masses of synchronised generators automatically store kinetic energy. This stored energy is available in the case of disturbances immediately to stabilise the system. As a consequence of the energy transition to RER the inertia will decrease continuously and may weaken thereby the resilience of the grids against disturbances severely. The current energy market design does not provide suffiicient sustainable incentives for such important system stabilising technologies [1]. The reason behind that is historical, since the conventional power plants did provide part of the necessary grid service automatically whenever it generated power. Therefore, it is necessary to find out how the resilience of the system can be guaranteed, in the future.

Since DC-AC converters of wind- and photovoltaic-generators feed their power directly into the grid and do not provide inertia of rotating masses to the grid, they have to be enabled technically to provide momentary reserve, as can be achieved by installing virtual synchronous machines. Therefore, we aim to study the response of the transmission grid to disturbances under these new conditions. To this end we investigate the spreading pattern of various kinds of disturbances in realistic transmission grid models. In particular we consider the Nigerian 330 kV transmission network, the Ghanaian 161 kV transmission network as well as the well known IEEE 118 bus test- 138 kV grid. In addition, we study model grids with a Cayley-tree topology, and a Square-Grid topology, where the substations are modeled with the same parameters as the Nigerian 330 kV transmission network. This investigation takes into account the topology of these grids with emphasis on their degree of meshedness, the power capacity of the transmission lines [2], momentary reserve power (in units of MW) as well as different grid inertia H (in units of seconds) in order to investigate quantitatively their influence on frequency dynamics of the grid. The spatial propagation of disturbances is investigated by measuring the time of arrival of a disturbance (t), as measured from the time t_0 when the disturbance occurred first, from which we would trace the travel pattern and subsequently the travel velocity of the disturbance.

II. Description, Modeling and Simulation of Electrical Power Networks

Let us start with the basic description of the five different network models used in the frequency dynamics investigations for the purpose of understanding the influence and interplay of system parameters and their contributions to the stability of the electrical power network.

A. The Nigerian Transmission Network Model

The Nigerian 330 kV transmission network comprises a total of 71 buses (substations/power terminals), 81 overhead transmission lines made from an alloy of aluminium and steel (with a limiting current of 1320 A) of which some consist of 2 or 3 circuit pairs. There are 107 less-decommissioned Unit generators which form the existing 29 power plant stations with a total power capacity of about $13,208MW$.

Kosisochukwu P. Nnoli is with the Department of Computer Science and Electrical Engineering, Jacobs University Bremen, 28759 Bremen, Germany (e-mail:k.nnoli@jacobs-university.de).

Stefan Kettemann is with the Department of Physics and Earth Science, and the Department of Computer Science, Jacobs University Bremen, 28759 Bremen, Germany, and also with the Division of Advanced Materials Science, Pohang 790-784, South Korea (e-mail:s.kettemann@jacobs-university.de).

The other voltage infrastructures include 132 kV, 66 kV (specifically for industrial utilities) and 33 kV sub-transmission networks. There are also 11 kV and 0.415 kV 3-phase distribution networks (for home and office utility areas). The Nigerian network is of ring topology where all the nodes are connected to one another in such a way that they form a closed loop prior to step-down [3], as seen in the single or one-line diagram of the Nigerian transmission network shown in Fig.1. All 330 kV voltage level buses, generators, controllers, and shunt compensators are represented [4].

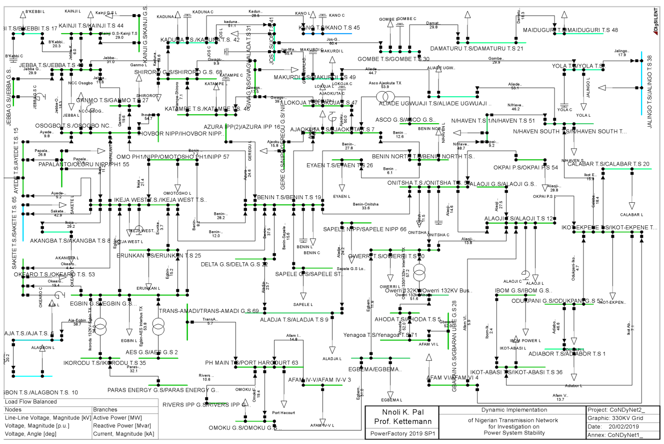

Fig. 1: Single-Line Diagram of the Nigerian 330 kV Transmission Network

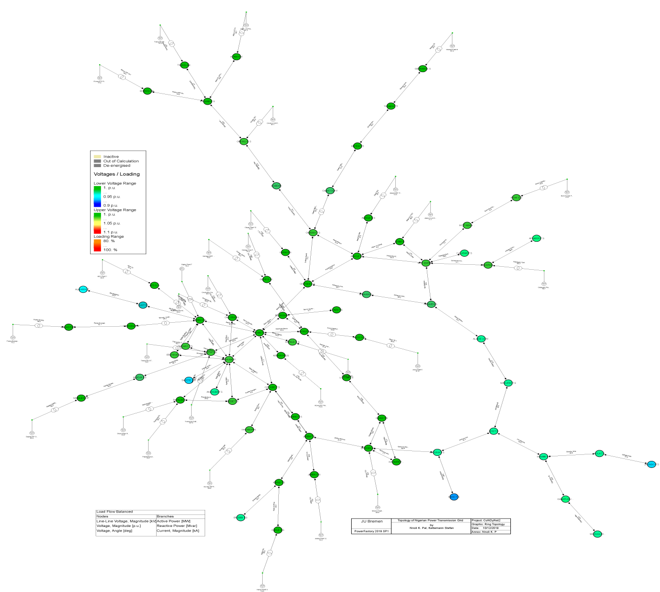

Fig. 2: The Topology of the Reduced Nigerian 330 kV Transmission Network with $N_S = 71$ buses.

For the purpose of simplifying this network with respect to the number of generating units and to allow a comparison with other network topologies without loosing their technical detailing and implications, we use in the following a reduced Nigerian 330 kV transmission network comprising of the 29 power plant stations with $N_S = 71$ buses with their individual units integrated, as shown in Fig. 2 and listed and enumerated in Appendix A and in Table IV.

B. The Cayley-Tree and Square Grid Transmission Model

In order to enable a comparative study with power grids of different topology, we use a Cayley-tree topology and a Square grid topology, where the substations are modeled with the same parameters as the Nigerian 330 kV transmission network and we choose the number of substations to be comparable. We use a Cayley-tree transmission network of branching number $b = 3$ and $M = 3$ generations, resulting in a total of N_S = 1+ 4 + (4 x 3) + (4 x 3 x 3) = 53 buses [2]. Note that $M = 4$ generations would give $N_S = 90$, exceeding the number of substations in the Nigerian power grid with $N_S = 71$. The other buses, loads, network shunt compensators and power injections were assigned starting from the beginning. See Appendix A and Table IV for details of these mappings. The power capacity, network loading, number of generating stations and other network parameters of the Cayley-tree network is chosen the same as in the Nigerian transmission network model. The single-line diagram of the Cayley-tree transmission network is shown in Appendix B in Fig. 21 while its tree-like topology is shown in Fig. 22.

The Square power grid is modeled with N_S= 8 x 8 = 64 buses with the remaining loads, shunt compensators and power injections added, recounting *from the beginning* as in the case of Cayley-tree network. This process enables the comparison of the Square power network model with the Nigerian model ensuring frequency and voltage tolerances according to [5]. The single line diagram and the topology of Square transmission grid are shown in Appendix B in Fig. 23 and Fig. 24 respectively. See also Appendix A and Table IV for details of these mappings.

C. The Ghana Power Transmission Model

Building on the results of [6] and with the recent developments in the Volta River Authority that maintains the power systems in Ghana, the Ghana transmission network comprises mostly of 161 kV high voltage transmission lines with only a few 330 kV and 225 kV line injections from neighbouring countries. At the moment, the total power capacity of the Ghana-grid is approximately $4,888MW$ with about 90 overhead transmission lines connecting 74 buses [7]. The Ghana transmission network comprises about 7 hydro-powered plants and 8 gas-powered plants. The single line diagram and the topology of Ghana transmission grid are shown in Figs. 3 and 4 respectively.

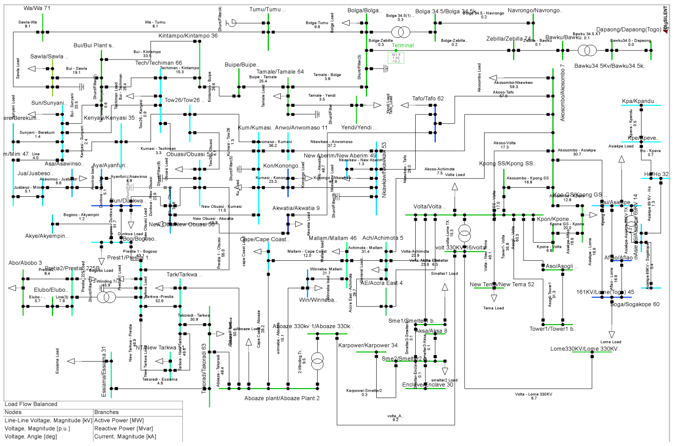

Fig. 3: Ghana Transmission Network Single-Line Diagram

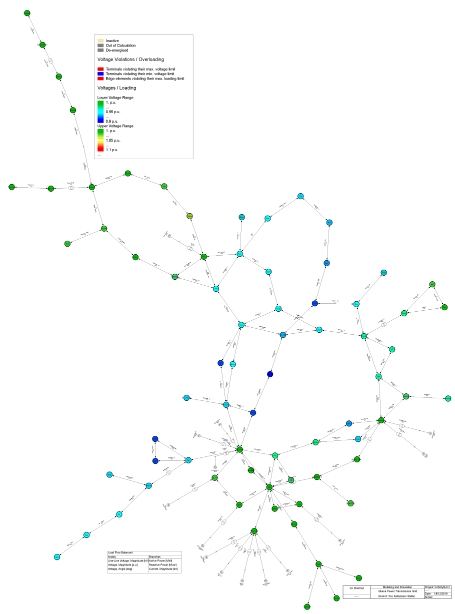

Fig. 4: Ghana Transmission Network topology with $N_S = 75$ buses.

D. The IEEE 118 Bus Test-Grid Model

The IEEE 118-bus test-grid used depicts an approximation of the American Electric Power system (in the U.S. Midwest) as of December 1962. The IEEE 118-bus system is made up of 19 synchronous generators, 35 synchronous condensers, 169 transmission lines of which few consist of double circuits, 9 inter-bus transformers, and 91 loads [8] [9]. The total power capacity of both the power plants and the synchronous condensers in this network is about $4882MW$ with a reserve of about $1069.33MW$. The one-line diagram and the topology of IEEE 118-bus test-grid are shown in Fig. 5 and Fig. 6 respectively.

The following transmission line parameters are used in the modeling of the Nigerian, Cayley tree, Square, Ghana and IEEE 118 Bus test power grid: the line connections (i.e. from terminal i to terminal j), number of circuits (pair number), lengths (in km), positive and zero sequence resistance ($R1$ and $R0$), reactance ($X1$ and $X0$), capacitance ($C1$ and $C0$), susceptance ($B1$ and $B0$) and rated current I_{rated}. Included are also their respective synchronous machines and/ condensers describing their active (P), reactive (Q), and apparent (S) powers and power factor (pf) [3] [4] [6] [7] [8].

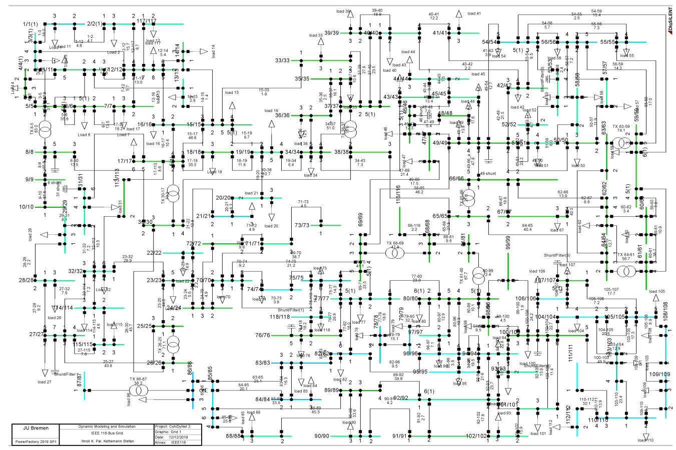

Fig. 5: Single-Line Diagram of IEEE 118-Bus Test-Grid

E. The Swing Equation and the Control Devices for the Network Power Plants

The devices used to control the outputs of the synchronous generating-units in all the grids include, but are not limited to, the automatic voltage regulator (AVR), responsible for voltage control of the generator through its excitation control. The speed governor used in the model is the turbine governor (TGOV-model) of the generator's prime mover which is responsible for keeping the generator's rotor frequency synchronous to the frequency of the grid, thereby maintaining the frequency operational limits when there are contingencies. The swing equation describes the balance between the mechanical torque T_m in N.m. of the plant's individual turbines and the electromagnetic torque T_e in N.m. of their synchronous generators, as governed by the differential equation [10] [11] [12],

$$J_i \frac{d\omega_i^R}{dt} + D_{wi}\omega_i^R = T_m - T_e, \tag{1}$$

where D_{wi} accounts for the rotational loss due to windings for the generator at bus i in N.m.s. Here i denotes the index of power generators in the grid, t time in seconds, $J_i = \frac{2H_i}{\omega_0^2}S_i$ is the combined moment of inertia of the turbine and generator in kg.m^2 with H_i the generator inertia constant in seconds and S_i the generator apparent power in volt-amperes (VA). Also, ω_i^R is the angular velocity of the rotor in electrical rad/s and ω_0 is its rated synchronous value in electrical rad/s. We assume that any change in the rotor's angular velocity $\omega_i^R - \omega_0$ is a derivative of its angular position δ (in electrical radians with respect to its synchronously rotating setpoint δ_0), given by

$$\omega_i^R - \omega_0 = \frac{d\delta_i}{dt}. \tag{2}$$

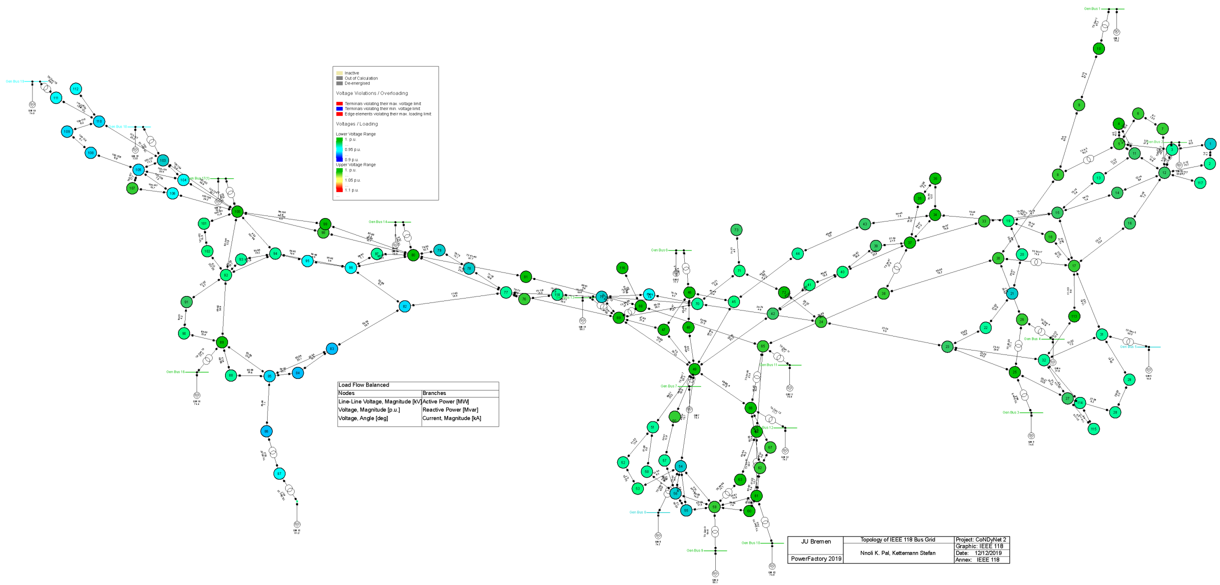

Fig. 6: The Topology of IEEE 118-Bus Test-Grid

Taking the derivative of ω_i^R with respect to time, we get,

$$\frac{d\omega_i^R}{dt} = \frac{d}{dt}\Big(\frac{d\delta_i}{dt}\Big) + \frac{d\omega_0}{dt}. \tag{3}$$

Since ω_0 is a constant rated synchronous value, Eq.(3) becomes

$$\frac{d\omega_i^R}{dt} = \frac{d^2\delta}{dt^2}. \tag{4}$$

In reality, ω_0 is related to the grid frequency v_o by $2\pi v_o$, where v_o could be 50 or 60Hz depending on a country's grid code. Substituting Eq.(4) into Eq.(1), we then have,

$$J_i\frac{d^2\delta_i}{dt^2} + D_{wi}\Big(\frac{d\delta_i}{dt}\Big) = T_m - T_e. \tag{5}$$

The assumption here is that the perturbation in the network effected on the rotors from the initial position is small. Multiplying both sides of Eq.(5) by the rated speed ω_0 in order to ensure that we maintain a uniform or synchronous speed throughout the system, balancing the power, we have

$$J_i\omega_0\frac{d^2\delta_i}{dt^2} + D_{wi}\omega_0\Big(\frac{d\delta_i}{dt}\Big) = T_m\omega_0 - T_e\omega_0. \tag{6}$$

Since power is a product of torque and angular velocity, the right side of Eq.(6) can be rewritten as

$$J_i\omega_0\frac{d^2\delta_i}{dt^2} + D_{wi}\omega_0\Big(\frac{d\delta_i}{dt}\Big) = P_m - P_e, \tag{7}$$

where P_m is the mechanical power from the turbine and P_e is the electrical power from the generator's air-gap. If we denote the angular momentum of the rotor at rated speed with M_i (i.e. $M_i = J_i\omega_0 = \frac{2H_i}{\omega_0}S_i$) and also denote the damping coefficient at rated synchronous speed with D_i (i.e. $D_i = D_{wi}\omega_0$), the swing equation can be written as

$$M_i\frac{d^2\delta_i}{dt^2} + D_i\Big(\frac{d\delta_i}{dt}\Big) = P_m - P_e, \tag{8}$$

and also as [13] [14] [15],

$$\frac{2H_i}{\omega_o}S_i\frac{d^2\delta_i}{dt^2} + D_i\frac{d\delta_i}{dt} = P_i + \sum_{j=1}^{N_S} K_{ij}\sin(\delta_j - \delta_i). \tag{9}$$

N_S is the number of nodes/buses, P_i is the power in the grid's i^{th} node. K_{ij} is the power capacity of the transmission lines which depends on the voltage. $(\delta_j - \delta_i)$ are phase differences. The control devices for the power plants also comprise the power system stabilizer (PSS) which is tasked with reducing the oscillatory instability and enhancing the damping of the entire power system's oscillations through excitation control. The controlled signal is a derivative of generator's rotor speed injected to the AVR through the excitation system to cancel out the phase lag between exciter's voltage set reference and the generator's windings torque [16]. In a basic power plant frame, it is also important to add over-excitation limiter (OEL) and the under-excitation limiter (UEL) for the AVR device, but we carry out the stability studies of the networks without the OEL and UEL devices as many power plants stations may not have them.

The choice of the synchronous machine models are based on IEEE guide for synchronous generator modeling practice and applications in power system stability analysis [17].

The turbine governor models used in the design simulations were chosen according to IEEE recommendations for dynamic models of turbine-governor in power system studies [18]. The following two models were used for the Nigerian, Cayley-tree, Square and Ghanaian power networks and the synchronous condensers part of IEEE 118-bus network: 1. The HYGOV model was used for the hydro power plants. 2. the simplified TGOV1 model was used for the thermal plants. The operations and basic signals are the same in both models. The excitation voltages of the synchronous generators in the networks are controlled by the simplified excitation (SEX-AVR) model and serve as their excitation and voltage control system except for the part of the synchronous generators in the IEEE 118 bus test-grid where the primary IEEET1-AVR model was used.

The choice of the automatic voltage regulator for synchronous generators was influenced by ENTSO-E [19]. The PSS2A model was used for all power plants in the networks. Each was tuned to ensure that no destabilising signal is fed back into the excitation system voltage summation point. Power system stabilizers remain the most cost efficient way of enhancing the damping of power system oscillations. The PSS2A standard model used in this design was influenced by IEEE recommended practice for excitation system models for power system stability studies [20].

III. Load Flow and Electromechanical Transient Stability Analysis in PowerFactory

Load flow calculation in complex power grids is used to determine voltage magnitude V and angle (θ) of the substations/buses, as well as the active (P) and reactive (Q) power [10]. In this design, DigSILENT PowerFactory is used to implement the Newton-Raphson (power equation, classical) method as its non-linear equation solver because of its fast-convergence. This method is used to obtain the initial conditions during the top of the maximum power flows in the entire power grids. The currents at steady state are calculated from

$$I_i = \frac{S_i^*}{V_i} = \frac{P_i + jQ_i}{V_i}, \tag{10}$$

where $i = 1, 2, \ldots, N_G$ and j the imaginary unit. Here, N_G is the total number of generators in the generating stations. The currents at the substations can be represented by the equation in admittance matrix form as,

$$I_{\mathrm{bus}} = Y_{\mathrm{bus}} V_{\mathrm{bus}}. \tag{11}$$

All dynamic components of the plants (AVR, PSS, Turbine / GOV models) and all system parameters were modeled and simulated. The active power balance is ensured by direct coupling of the grid frequency $50/60Hz$ to the synchronous generators, ensuring inertia activation and nodal relaxations. The phase coupling between the generators is described by the classical swing equation model with frequency-dependent load damping. The effect of increasing the injection of renewable energy resources on the stability of the electrical power networks based on the classical swing equation is studied on these power grids by varying the aggregated inertia constant H_{grid} of the entire grid by [21],

$$H_{\mathrm{grid}} = \frac{\sum_{i=1}^{N_S} H_i S_i}{S_T}. \tag{12}$$

where $S_T = \sum_{i=1}^{N_S} S_i$ is the total rated apparent power in the grid, S_i and H_i are the rated power and the inertia constant of the i^{th} node/bus respectively. Note that H_i on non-generator buses are set to zero. The data of the various grids used in this analysis are summarised in Table I.

A. Transient Dynamic Analysis

The voltage profiles from the stationary power flow of the grids were examined at no transient to investigate whether the buses actually maintained their realistic voltage tolerance according to the Nigerian grid code. The Nigerian grid code specifies voltages of 0.85 p.u. minimum (i.e. 280.5 kV) and 1.05 p.u. maximum (i.e. 346.5 kV) tolerances for the buses. For the frequencies, the grid code specifies frequencies of 0.995 p.u (min) and 1.005 (max) tolerance for network elements where frequencies of 0.99 p.u. (min) and 1.01 p.u. (max) are used in actual daily operational procedure [5]. The voltage profiles of the Nigerian, Square, Cayley-tree, Ghana and IEEE 118 test power networks at steady operating conditions (undisturbed operation) were captured and respectively represented in bar-charts in Appendix C. The results show that the buses were all within the specified voltage tolerance. Overloading of power generators is defined to be any loading above 80% which we therefore choose as our maximum loading thresholds. The magnitude of the injected perturbations P_{inj} for the synchronous machine (SM) events are chosen such that the studied power grids are comparable. We choose it to be

$$P_{\mathrm{inj}} = 0.5 \frac{P_T}{N_{\mathrm{PV}}}, \tag{13}$$

where $P_T = \sum_{i=1}^{N} P_i$ is the total active power in the grid and N_{PV} the total number of generator buses participating in the power injections, as given in Table I. A PV bus is a bus from which generator(s) are connected to the power system.

TABLE II: Injected-Perturbations in the Grids

tylePerturbation P_{inj}	Nigerian	Square	Cayley-Tree	Ghana	IEEE 118
SM-Event (MW)	264	300	314	349	115

A comparison chart showing the amount of power in MW that participated in the SM-Event is shown in Table II.

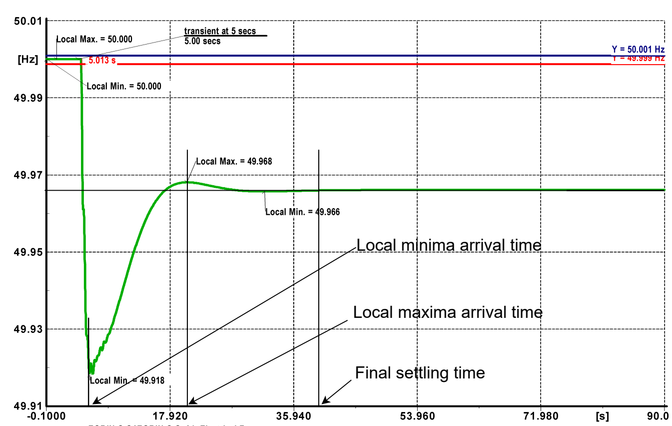

Fig. 7: Green Line: Frequency as a function of time at a bus where a Synchronous Machine (SM) Event occurs at $t = 5s$. Blue line: Frequency deviation threshold at 50.001 Hz. Red Line: Deviation threshold at 49.999 Hz.

These outage contingencies were simulated at the power plants substations which were chosen to have the minimum

TABLE I: Grid Parameter Values

Grid Data	Nigerian	Square	Cayley	Ghana	IEEE
Total Active P_T (MW)	13208	13208	13208	4888	4374
Total Rated S_T (MVA)	15450	15450	15450	5525	5112
Grid Voltage,V (KV)	330	330	330	161	138
Number of Lines N_L	81	112	52	90	169
Avg. Line-Length, a (Km)	92	100	100	59	46
Number of PV buses N_{PV}	25	22	21	7	19
Number of Gen Stations N_G	29	29	29	14	19
Number of Substations/buses N_S	71	64	53	74	118
Total Number of Effective buses $N_{\mathrm{r_{eff}}}$	25	22	21	7	54
Avg.Line-Inductance L per length (mH/Km)	1.076	1.054	1.054	1.332	1.292

geodesic distances to the rest of the substations for each grid so that they are most centrally located and the spread of disturbances throughout the grid can be monitored. As shown in Fig.7, the threshold meter used to monitor the arrival of frequency deviations was placed at very small values of $\pm$ 0.001 Hz, in order to record the direct spread of the disturbances. The synchronous machine event occurred at exactly $t_0 = 5s$ in the $90s$ transient electromechanical stability simulation time frame. The switching at the event took a finite time of $\Delta t = 200$ ms. The IEEE 118 Bus test-grid has a nominal $\nu_0 = 60$ Hz frequency. All other grids have $\nu_0 = 50$ Hz as nominal frequency. In the simulations we choose not to include any controller at the power plants, in order to be able to focus the investigation on the contribution of grid inertia on the disturbance spreading pattern and speed. In Figs. 8 to 14, we show the results of the measurement of the arrival time of the disturbance at each bus in the grids, after the event at time t_0, as obtained in the simulation with PowerFactory. That arrival time t is defined as the time, when the frequency first deviates by more than the threshold deviation $\delta\nu = \pm.001$ Hz from the nominal frequency ν_0.

In Fig. 8, the arrival times are shown as function of the geodesic distance r from the event location for different aggregated grid inertia of $H_{\mathrm{grid}} = 2s, 4s, 6s, 8s$. The grid inertia was varied by multiplying all H_i by the same factor. First of all, we see that the arrival times tentatively increase with the geodesic distance r from the event location. Secondly, we find that the arrival times are spread over a wider range as the inertia H_{grid} is increased. If the propagation would be ballistic, that is the perturbation spreads with a definite velocity v, the arrival time t after the disturbance starting from the time of disturbance t_0 would be linearly related to the distance r as,

$$t = b_0 + \frac{r}{v}. \tag{14}$$

The Table III shows the result for the linear regression parameter b_0 which is used to fit the arrival time as function of geodesic distance in the various power grids to the ballistic equation Eq. (14), shown as magenta lines in Figs. 8 to 14. The

Grid	H_{grid}(s)	b_0(s)
Nigerian	2	5.0130
	4	5.0133
	6	5.0132
	8	5.0133
Cayley-Tree	2	5.0150
	4	5.0149
	6	5.0149
	8	5.0148
Square	2	5.0134
	4	5.0137
	6	5.0137
	8	5.0137
Ghana	2	5.0012
	4	5.0012
	6	5.0012
	8	5.0007
IEEE 118 Bus	2	5.0130
	4	5.0133
	6	5.0134
	8	5.0135

TABLE III: The Regression values for the Frequency Dynamics Curve-Fit

parameter b_0 is found to be typically larger than the actual time $t_0 = 5.0s$ when the disturbance occurred, which can be due to the fact that the synchronous machine contingency may have a small delay, and the switching takes a small time $\delta t = 200ms$.

In order to better understand these results, let us compare them with results obtained by the solution of the swing equation Eq.(9). For homogeneous parameters and assuming purely inductive transmission lines, which is a good assumption for high voltage transmission lines, one can solve the swing equations analytically. For meshed grids and sufficiently large inertia one finds in linear response theory that a disturbance spreads ballistically according to Eq. (14) with a velocity $v = \sqrt{K/(\omega_0 J)}a$, where a is the length of a transmission line [2], [22]. Here J is the inertia of a synchronous generator or motor, respectively, where it is assumed that the inertia is the same at every node. In real power grids all parameters are inhomogeneous, that is the power capacity K_{ij} and the length a_{ij} are different for every transmission line between node i and j, and the inertia J is different for every generator J_i, with some of the nodes having no inertia. In an attempt to compare if the velocity in a real grid has a similar parametric

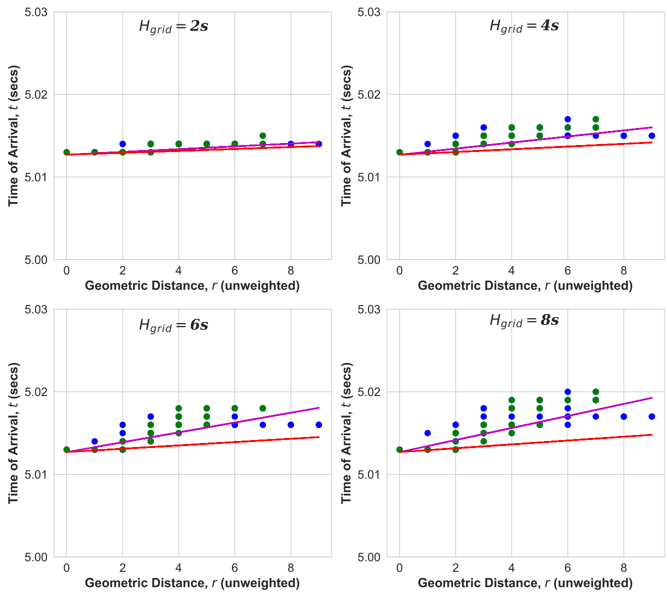

Fig. 8: Time of arrival of disturbance versus geodesic distance for the Nigerian Power grid from results of transient dynamic simulations for different inertia parameter H_{grid}. Green dots: arrival time(s) at bus(es) with at least one inertia injection. Blue dots: arrival time(s) at bus(es) with no inertia. Magenta line: fit to ballistic Eq. (14). Red line: ballistic Eq. (14) with velocity calculated according to Eq. 15.

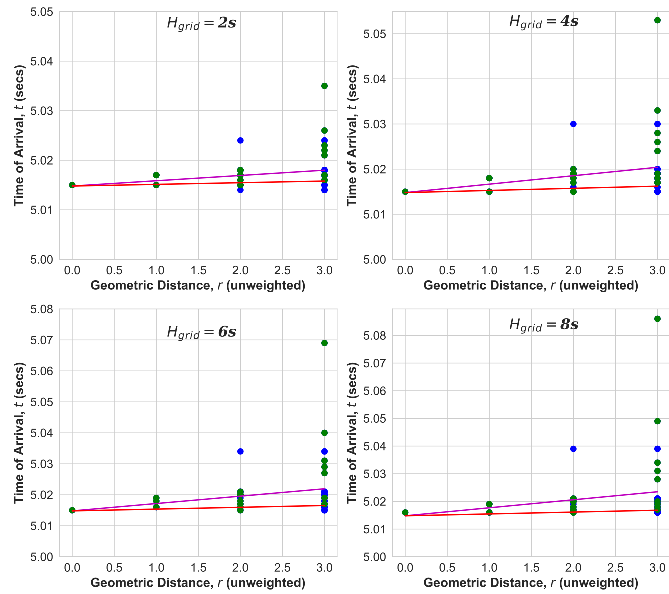

Fig. 9: Time of arrival of disturbance versus geometrical distance for the Cayley-Tree Power grid from transient dynamic simulations for different inertia parameter H_{grid}. Green dots: arrival time(s) at bus(es) with at least one inertia injection. Blue dots: arrival time(s) at bus(es) with no inertia. Magenta line: fit to ballistic Eq. (14). Red line: ballistic Eq. (14) with velocity calculated according to Eq. 15.

dependence let us therefore define a velocity in terms of average parameters

$$v_{\text{eff}} = \sqrt{\frac{\bar{K}\omega_0}{2H_{\text{grid}}S_B}}\,\bar{a}, \tag{15}$$

where $\bar{K} = \sum_{i<j} K_{ij}/N_L$, where N_L is the total number of transmission lines in the grid. Here, $K_{ij} = V^2/(\omega_0 L_{ij})$ is the power capacity of a purely inductive transmission line between nodes i and j, V is the voltage and L_{ij} is the line positive sequence inductance. $\bar{a}$ is the average length of the transmission lines. H_{grid} is the aggregated inertia constant in Eq. (12). $S_B = S_T/N_S$ is the total rated grid power in units of MVA divided by the total number of nodes/buses N_S. With these definitions we are now ready to compare with the simulation results by PowerFactory, which is based on swing equations in the realistic electricity networks with inhomogeneous parameters. We plot there also Eq.(14) (red line) using the analytical averaged velocity Eq. (15) in Figs. 8 to 15. The parameter b_0 is fitted as given in Table III.

We observe for the Nigerian power grid in Fig. 8 that the ballistic Eq. (14) with the velocity calculated according to Eq. 15 (red line) provides a lower bound for the time of arrival for all nodes and for all inertia $H_{\text{grid}} = 2s, 4s, 6s, 8s$.

The actual measured arrival times t are found to be spread in an interval $r/v_{eff} < t - b_0 < r/v_{min}$, where the width of this interval is found to increase with inertia. Thus, we find that the minimal velocity of the disturbance v_{min} decreases with increasing inertia. This can be understood by the fact, that the parameters are inhomogenous. Let us therefore explore the

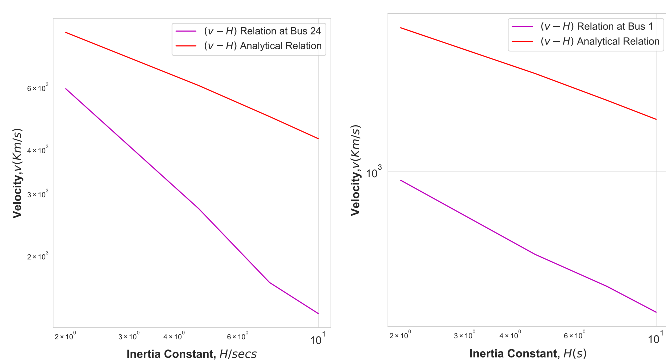

Fig. 10: Fitted ballistic velocity v as function of inertia constant H (Magenta Line), and the velocity according to the analytical Eq. (15) (red line), for the Nigerian Power Grid Fig. 8 (left) with contingency at bus 24 and for the Cayley Tree Grid, Fig. 9 (right) with contingency at bus 1 in double logarithmic plot.

effect of the inhomogeneous distribution of the inertia further. In Fig. 8 the arrival times at buses with no inertia are plotted in blue, while the green dots indicates that at least one of the buses at this distance and with this arrival time has inertia.

The fact that the propagation of the disturbance is delayed in nodes with inertia while in nodes without inertia it propagates without delay, can be seen in Fig. 8, in particular for the example of the bus at distance $r = 9$, where the disturbance arrives at the same time as at the node at distance $r = 8$, which has no inertia.

For the Cayley-tree power grid, we observe in Fig. 9 that

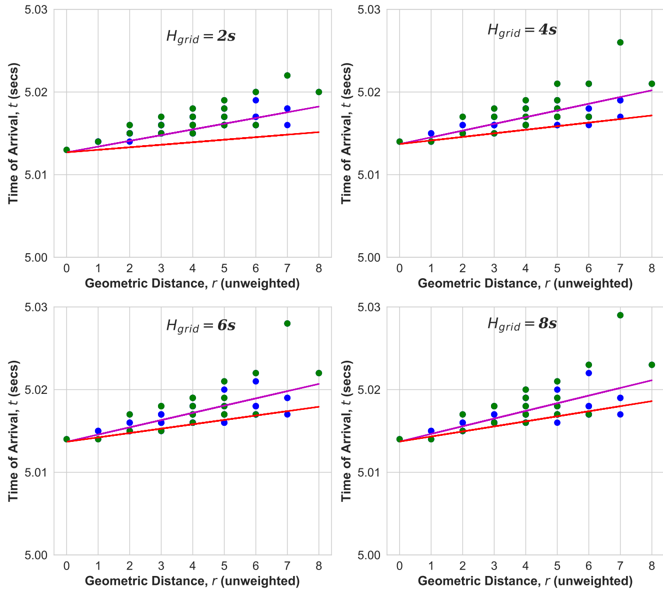

Fig. 11: Time of arrival of disturbance versus geodesic distance for the Square Power grid as obtained by transient dynamic simulations for different inertia parameter H_{grid}. Green dots: arrival times at buses with at least one inertia injection. Blue dots: arrival times at buses with no inertia. Magenta line: fit to ballistic Eq. (14). Red line: ballistic Eq. (14) with velocity calculated according to Eq. 15.

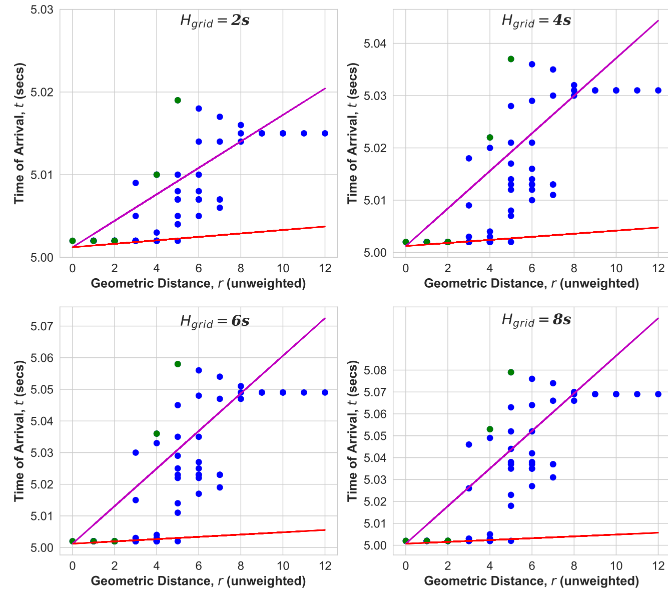

Fig. 12: Time of arrival of disturbance versus geodesic distance for the Ghana Power grid as obtained from transient dynamic simulations for different inertia parameter H_{grid}. Green dots: arrival times at buses with at least one inertia injection. Blue dots: arrival times at buses with no inertia. Magenta line: fit to ballistic Eq. (14). Red line: ballistic Eq. (14) with velocity calculated according to Eq. 15.

the ballistic Eq. (14) with the velocity calculated according to Eq. 15 no longer provide a lower bound for the time of arrival for all buses. The lower the inertia H_{grid}, the more outliers there are, which are the data points which fall below the red line. This can again be explained by the lack of inertia in some of the buses, f.e. the fact that the bus at distance $r = 2$ with smallest time of arrival has no inertia, as indicated by the blue colour, explains that the disturbance arrived at almost the same time, at a bus at distance $r = 3$.

In Fig. 10 we show the double logarithmic plot of the fitted ballistic velocity (magenta) and the analytical velocity (red) versus the inertia constant H for the Nigerian power grid (left) and the Cayley tree grid (right). We observe that the fitted velocity decays with the inertia in both power grids faster than the analytical velocity which decays with the power law $\sim H^{-1/2}$.

In the Square grid shown in Fig.11, we observe that the ballistic Eq. (14) with the velocity calculated according to Eq. 15 does provide a lower bound for the time of arrival for all buses, only for the smallest inertia $H_{\mathrm{grid}} = 2$, while there are outliers at higher H_{grid}.

Fig.12 shows the result for the time of arrivals as function of the geodesic distance in the Ghana grid. The ballistic Eq. (14) with the velocity calculated according to Eq. 15 (red line) does provide a lower bound for the time of arrival only at small and large distance, while there are outliers for all values of H_{grid} at intermediate distances $r = 2, ..., 5$). In addition, we observe that there is a wide spreading of the time of arrivals at intermediate distance from the point of contingency which increases with corresponding increase in the H_{grid}. We note

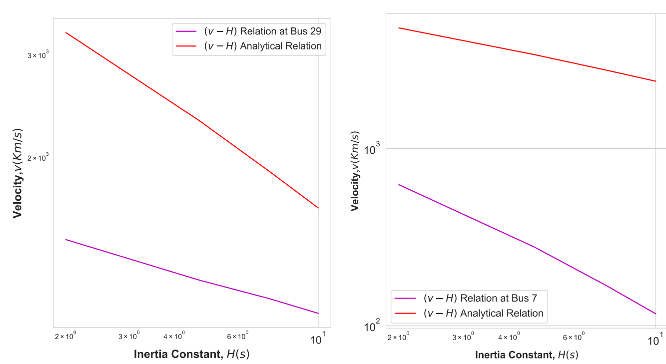

Fig. 13: Fitted ballistic velocity v as function of inertia constant H (Magenta Line), and the velocity according to the analytical Eq. (15) (red line), for the Square Power Grid Fig. 11 (left) with contingency at bus 29 and for the Ghana Power Grid, Fig. 12 (right) with contingency at bus 7 in double logarithmic plot.

that the Ghana grid is highly connected with ring like topology at the center of the grid, while there are tree like connections to outer buses. This may explain the wide spreading of arrival times.

In Fig. 13 we show the double logarithmic plot of the fitted ballistic velocity (magenta) and the analytical velocity (red) versus the inertia constant H for the square power grid (left) and the Ghana grid (right). We observe that the fitted velocity decays with the inertia in the square power grid more slowly than the analytical velocity which decays with the power law $\sim H^{-1/2}$, while in the Ghana grid, the fitted velocity decays with the inertia as in the square power grid with a power law, but faster than the analytical velocity.

In the IEEE 118-bus test grid shown in Fig.14, we observe that v provides a good lower bound for the disturbance dispersion in the ballistic path (red line) only for the lowest inertia value $H_{\rm grid} = 2s$. For higher inertia, there are outliers at intermediate geodesic distances. Here, the spreading of the time of arrivals are smaller than in the other grids. This may be because of the high degree of meshedness of this grid similar to what we observed in the square grid in Fig. 11.

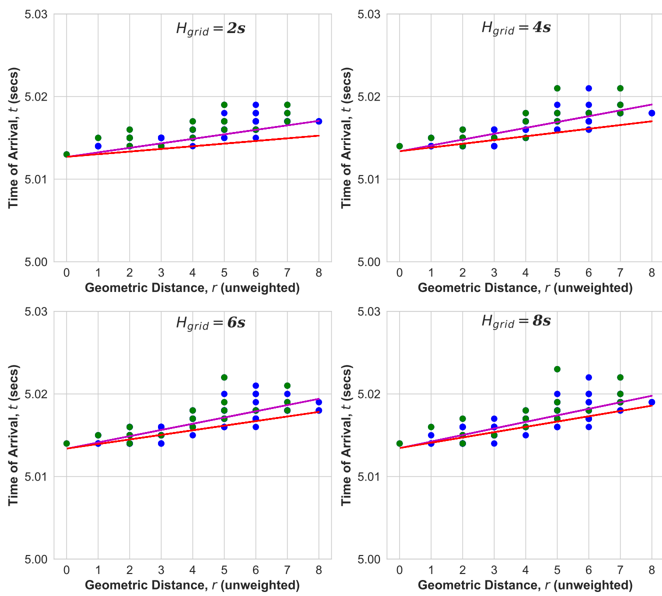

Fig. 14: Time of arrival of disturbance versus geodesic distance for the IEEE 118 Bus Power grid as obtained from the transient dynamic simulations for different inertia parameter $H_{\rm grid}$. Green dots: arrival times at buses with at least one inertia injection. Blue dots: arrival times at buses with no inertia. Magenta line: fit to ballistic Eq. (14). Red line: ballistic Eq. (14) with velocity calculated according to Eq. 15.

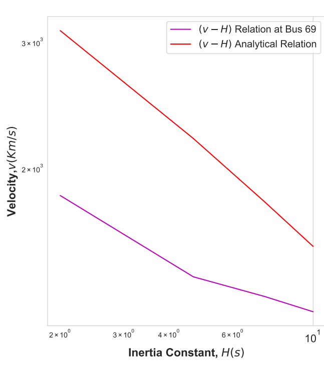

Fig. 15: Fitted ballistic velocity v as function of inertia constant H (Magenta Line), and the velocity according to the analytical Eq. (15) (red line), for the IEEE Power Grid Fig. 14 with contingency at bus 69 in double logarithmic plot.

In Fig. 15 we show the double logarithmic plot of the fitted ballistic velocity (magenta) and the analytical velocity (red) versus the inertia constant H for the IEEE 118-bus test grid. We observe that the fitted velocity decays with the inertia more slowly than the analytical velocity which decays with the power law $\sim H^{-1/2}$.

In summary, we conclude that the more meshed a power grid is, that is the more loops it has, the weaker is the dependence of the spreading of the disturbance on the grid inertia $H_{\rm grid}$. This can be seen from the weaker dependence of the ballistic velocity on the inertia in both the square grid and the IEEE 118-bus test grid. Moreover we observe that in more tree like grids there is a wider spread of arrival times, and in particular there are buses where the disturbance arrives much later than expected in a meshed grid. This observation is in accordance with the result of Ref. [2], where it was found that a disturbance tends to be more easily localised in a tree like grid, preventing or at least slowing down its spreading. Thus, the response to the contingency is in some buses slower in the less meshed grid, like the Cayley-tree and the Ghana grids, as compared to the more meshed grids like the square grid Fig. 11 and the IEEE grid Fig. 14.

In order to better account for the lack of inertia in some of the buses, one could introduce an effective geodesic distance $r_{\rm eff}$ between the node i, where the disturbance started, to a node j in the power grid along a path $P_{ij} = \{i, k_1, k_2, .., j\}$, by counting only nodes $k_1, k_2, ...$ which contribute inertia H_{k_n}, $n = 1, ..., r^A_{\rm eff}$ to the network inertia $H_{\rm grid}$ (i.e. a generator or synchronous condenser injection node). Thus,

$$r^A_{\rm eff} = \text{Geodesic Distance } d(i, k_1, k_2, ..., j)|_{H_i, H_{k_n} \neq 0}. \quad (16)$$

However, the implementation of this formula, requires a reduction of the graph to the nodes with inertia, and thereby a change of the topology of the power grid.

Let us therefore rather introduce a properly weighted effective distance $r_{\rm eff}$. Extending the analytical result for the velocity as derived from the swing equations to the swing equations with inhomogenous parameters, we arrive at the following velocity or the disturbance when propagating between nodes i and j

$$v_{ij} = \min\left(\sqrt{\frac{K_{ij}}{J_i \omega}} a_{ij}, c_{ij}\right), \quad (17)$$

where a_{ij} is the length of this transmission line, and c_{ij} is the velocity of propagation along the transmission line between nodes i and j. In a transmission line, which has no or low Ohmic losses, the velocity along the transmission line c_{ij} can be derived from the effective wave equation of the transmission line, which has the form of the telegraph equation. One obtains it as a function of the inductance and capacitance of the transmission line [23] as $c_{ij} = 1/\sqrt{L_{ij} C_{ij}}$, yielding a result which is close to the velocity of light $c = 3{\rm x}10^8 m/s$ for high voltage transmission lines. Thus, the velocity along the transmission line, c_{ij} is typically much larger than the velocity, which is caused by the delay due to the momentary reserve of a bus at node i with inertia J_i Thus, when node i has inertia, we get $v_{ij} = (\sqrt{\frac{K_{ij}}{J_i \omega}} a_{ij})$. If there is no inertia in node i, $J_i = 0$, however, the disturbance spreads to the next node faster, with velocity c_{ij}, close to the speed of light. Thus, this explains the fact that the observed arrival times are spread widely, and that there are also nodes which are reached by the disturbance faster than expected in a homogeneous grid. According to Eq. (17) we expect that nodes which are connected with the location of the disturbance through nodes with low or no inertia are reached faster by the disturbance. Let us therefore try to take this fact into account. Using Eq. (17) we can give a more accurate estimate for the time of arrival at a node l when the disturbance occurs at node k by

$$t_{kl} - b_0 = \min \left(\sum_{\text{Path from k to l}} \frac{a_{ij}}{v_{ij}} \right), \tag{18}$$

where the sum is over all pairs of nodes i, j along that path between nodes k and l which has the minimal arrival time. The velocity v_{ij} is given by Eq. (17). Accordingly, we can now define an effective distance between nodes k and l by

$$r_{eff}^{kl} = \frac{v_{eff}}{a} \min \left(\sum_{\text{Path from k to l}} \frac{a_{ij}}{v_{ij}} \right), \tag{19}$$

where v_{eff} is the effective velocity defined in Eq. (15) and a the average transmission line length.

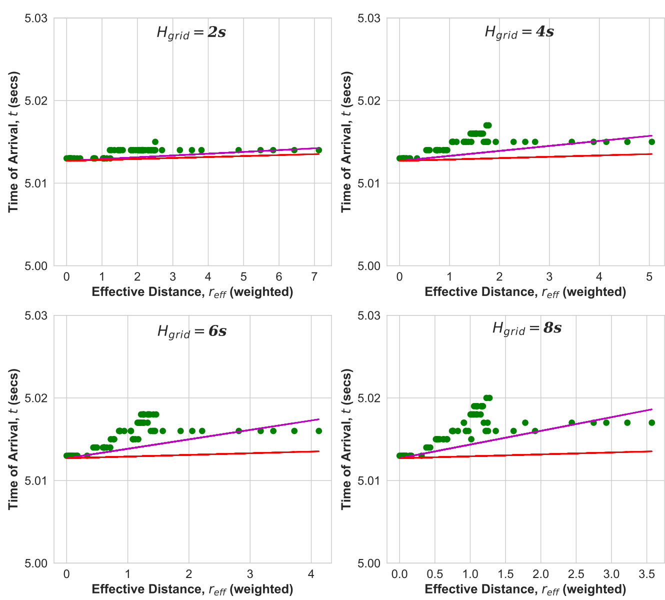

Fig. 16: Time of arrival of disturbance versus effective distance for the Nigerian Power grid according to Eq. (19) for different inertia parameter H_{grid}. Magenta line: fit to ballistic Eq. (14). Red line: ballistic Eq. (14) with velocity calculated according to Eq. (17).

Now, let us check whether plotting the measured arrival time versus this effective distance r_{eff}, we get a less scattered plot with fewer outliers. We consider in particular those grids where we observed many outliers, namely the Nigerian, Cayley-tree and Ghana power grid. In Fig. 16 we plot the times of arrival versus the r_{eff} for the Nigerian grid. We observe that the ballistic motion with the analytical velocity Eq. (15) provides now a strict lower bound for all effective distances (red line). Also, the arrival times are more clustered as compared to the plot versus geodesic distances shown in Fig 8.

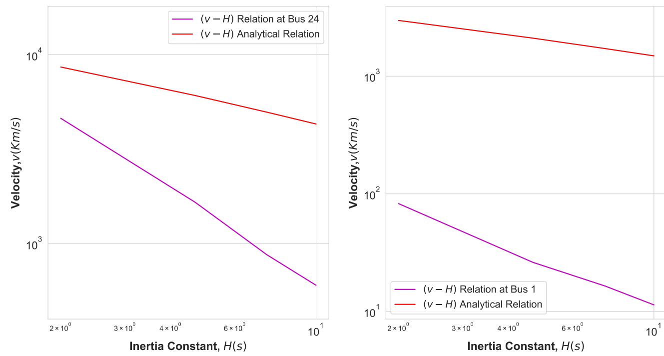

Fig. 17: Fitted ballistic velocity v as function of inertia constant H (Magenta Line), and the velocity according to the analytical Eq. (15) (red line), for the Nigerian Power Grid when the time of arrival is plotted against the effective distance, Fig. 16 (left) with contingency at bus 24 and for the Cayley Tree Power Grid, Fig. 18 (right) with contingency at bus 1 in double logarithmic plot.

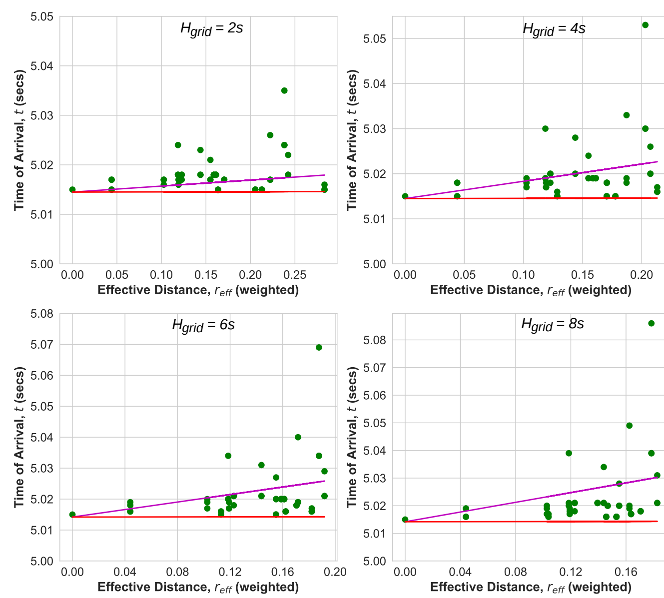

Fig. 18: Time of arrival of disturbance versus effective distance for the Cayley-Tree Power grid according to Eq. (19) for different inertia parameter H_{grid}. Magenta line: fit to ballistic Eq. (14). Red line: ballistic Eq. (14) with velocity calculated according to Eq. (17).

In Fig. 18, we plot the times of arrival versus the r_{eff} for Cayley tree power grid. We find also in this tree grid topology, that the ballistic motion with the analytical velocity Eq. (15) provides now a strict lower bound for all effective distances (red line). There remains however a wide distribution of the times of arrival without a strong correlation with the effective distance r_{eff}. In Fig. 17 the double logarithmic plot of the fitted ballistic velocity (magenta) and the analytical velocity (red) versus the inertia constant H is shown for the Nigerian power grid (left) and the Cayley tree grid (right). We observe that the agreement of the fitted velocity with a power law decay with inertia is in both power grids better as compared to Fig. 10, which was extracted from the plot versus geodesic distance. The power law decay is found to be faster than the analytical velocity which decays with the power law $v \sim H^{-1/2}$.

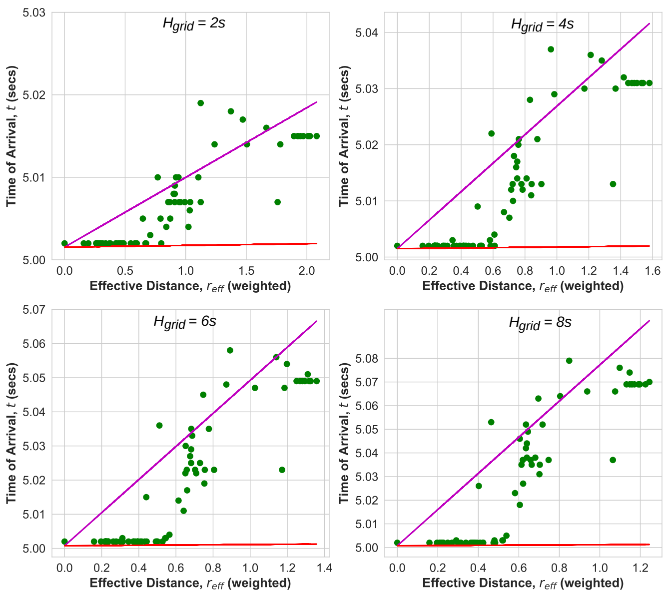

Fig. 19: Time of arrival of disturbance versus effective distance for the Ghana Power grid according to Eq.(19) for different grid inertia H_{grid}. Magenta line: fit to ballistic Eq. (14). Red line: ballistic Eq. (14) with velocity calculated according to Eq. (17).

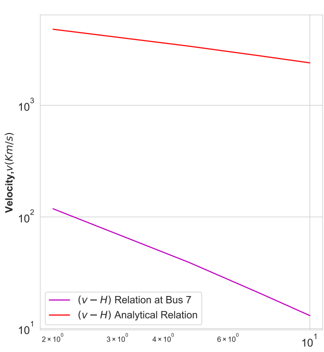

Fig. 20: Fitted ballistic velocity v as function of inertia constant H (Magenta Line), and the velocity according to the analytical Eq. (15) (red line), for the Ghana Power Grid Fig. 19 with contingency at bus 7 in double logarithmic plot.

The Fig.19 shows the result for the times of arrival as a function of the effective distance in the Ghana grid. In comparison with Fig.12, we observe that the times of arrival become more clustered with no outliers.

In Fig. 20 we show the double logarithmic plot of the fitted ballistic velocity (magenta) and the analytical velocity (red) versus the inertia constant H for the Ghana grid as obtained by fitting the times of arrival as a function of the effective distance shown in Fig. 19. We observe that the fitted velocity decays with the inertia in the Ghana power grid with a power law, but still faster than predicted by the analytical velocity $v \sim H^{-1/2}$.

In summary, we found that the plot of the arrival time versus effective distance r_{eff} shows a stronger correlation than with geodesic distance. The ballistic equation with analytical velocity Eq. (15) is found to provide a strict lower bound for all effective distances. The fitted velocity is found to decay with a power law, albeit with a faster decay than the one expected from the analytical velocity $v \sim H^{-1/2}$.

IV. Summary and Conclusions

The spread of a disturbance in transmission power grids was studied on different realistic network topologies by means of the DigSILENT PowerFactory commercial power software and compared with analytical results obtained from the swing equations. We find a strong dependence on the grid inertia and the degree of meshedness, which we have analysed systematically. By plotting the measured arrival time of a disturbance versus the geodesic distance from the location of the perturbation, we find only a weak correlation between these parameters. Lowering the inertia in the grid is found to reduce the time of arrival irrespective of the grid topology. Thus, the disturbances is found to travel faster with less inertia, or equivalently, with more RES in the grid. Moreover, we observe that in tree like grids, like the Cayley tree grid and grids with small meshedness, like the Ghana grid, there is a wider spread of arrival times, while in more meshed grids, like the Square and IEEE 118 Bus test power grids, there is a stronger clustering of arrival times versus distance and the disturbance decays faster.

Plotting instead the arrival time versus an effective distance r_{eff}, which we defined here in order to take into account the inhomogenous distribution of inertia, we find a much stronger correlation than with the geodesic distance. A ballistic equation for the arrival time with an analytical velocity, as derived from the swing equation, is then found to provide a strict lower bound for all effective distances. The fitted velocity is found to decay with a power law with the grid inertia.

These insights on the response of the transmission grid to disturbances under the new conditions when more wind- and photovoltaic- generators feed their power directly into the grid and do not provide inertia of rotating masses to the grid, may therefore help to better prepare the power grids for the energy transition.

Acknowledgment

We gratefully acknowledge the support of Bundesministerium für Bildung und Forschung (BMBF) CoNDyNet-2, FK. 03EK3055D.

References

[1] Energie-Forschungszentrum Niedersachsen, *Studie Eignung von Speichertechnologien zum Erhalt der Systemsicherheit FA43/12 Abschlussbericht*, 2013.

[2] S. R. Tamrakar, M. Conrath, and S. Kettemann, "Propagation of disturbances in AC electricity grids," *Scientific Reports 8*, vol. 6459, pp. 1-10, 2018.

[3] National Control Center Osogbo, "Transmission data update of the transmission company of Nigeria," 2019.

[4] K. P. Nnoli, “Implementation of a dynamic network model of the Nigerian transmission grid for investigations on power system stability,” *https://doi.org/10.31224/osf.io/r82zn*, 2019.
[5] Nigerian Electricity Regulatory Commission (NERC), *The Grid Code for the Nigerian Electricity Transmission System*. NERC Press, 2014.
[6] K. Mensah, “Improving stability of Ghana’s power system using power system stabilizer (PSS),” *Norwegian University of Science and Technology*, 2009.
[7] Ghana Volta Power Authority, “Transmission data updates from the Ghana Volta Power Authority,” 2019.
[8] Illinois Information Trust Institute, “IEEE 118 Bus Test Grid,” *[Online] http://energy.komisc.ru/downloads/schemes/ieee_118.txt*, 2012.
[9] R. D. Christie, “Power systems test case archive,” *http://labs.ece.uw.edu/pstca/*, 1999.
[10] P. Kundur, *Power System Stability and Control*, 1994.
[11] A. A. Sallam and O. P. Malik, *Power System Stability: Modelling, Analysis and Control*. IET Power and Energy Series 76, 2015.
[12] J. Machowski, J. Bialek, and J. R. Bumby, *Power System Dynamics: Stability and Control*, 2008.
[13] G. Filatrella, A. H. Nielsen, and N. F. Pedersen, “Analysis of a power grid using a kuramoto-like model,” *The European Physical Journal B*, vol. 61, no. 4, pp. 485–491, 2008.
[14] D. Manik, M. Rohden, H. Ronellenfitsch, X. Zhang, S. Hallerberg, D. Witthaut, and M. Timme, “Network susceptibilities: Theory and applications,” *Physical Review E 95, 012319*, 2017.
[15] A. R. Bergen and D. J. Hill, “A structure preserving model for power system stability analysis,” *IEEE Transactions on Power Apparatus and Systems*, vol. PAS-100, no. 1, pp. 25–35, 1981.
[16] G. Rogers, “Demystifying power system oscillations,” *IEEE Computer Applications in Power*, 1996.
[17] IEEE Power Engineering Society, *IEEE Guide for Synchronous Generator Modelling Practice and Applications in Power System Stability Analysis*. IEEE Press, 2002.
[18] IEEE Power and Energy Society, *Dynamic Models for Turbine-Governor in Power System Studies*. IEEE Press, 2013.
[19] ENTSO-E, *Documentation on Controller Test in Test Grid Configurations*, 2013.
[20] IEEE Power Engineering Society, *IEEE Recommended Practice for Excitation System Models for Power System Stability Studies*. IEEE Press, 1992.
[21] A. Ulbig, T. S. Borsche, and G. Anderson, “Impact of low rotational inertia on power system stability and control,” vol. Vol. 14(3), pp. 7290-7297, 2014.
[22] S. Kettemann, “Delocalization of disturbances and the stability of ac electricity grids,” *Phys. Rev. E 94, No. 062311*, (2016).
[23] M. Sadiku, *Elements of Electromagnetics [3 ed.]*, ser. Oxford Series in Electrical and Computer Engineering. Oxford University Press, 2000.

Appendices

Appendix A
Generation and Transformation of the Nigerian Network to Cayley-Tree and Square Grids

Here we present the details of our approach to transform the realistic Nigerian grid to the Cayley tree and the Square grid topology. The Cayley tree grid in Fig. 21 models a power network which is operated in a tree-like fashion to enable easier identification and repair network failures. There is an outward spread of links from a central substation terminal with branching number b_l, at branching generation l. It is furthermore characterized by the distance between neighbored substation terminals a and the total number of terminals N. The degree d_i, the number of branches connecting terminal i to any other terminal is for the Cayley tree network, $d = b+1$ except at surface edge substation terminals where $d = 1$. Here, we define $b = 3$ and $M = 3$ branching levels. In total, we have that N_S = 1 + 4 + (4 x 3) + (4 x 3 x 3) = 53 buses since we are mapping only 71 buses onto the tree network. Further mapping will result to an excess of 90 buses as we discussed in section II-B. However, there is no direct way to transform one node and all its links from Nigerian grid to the Cayley tree grid and still maintaining its tree-like nature, the exact connected terminals for each bus bar is therefore neglected. The Nigerian network is then re-arranged into Cayley tree using the Nigerian bus identities (I.D. i.e. 1, 2, 3 ... 53) as shown in Table IV along the tree-like topology starting from the middle bus and still maintaining their individual nodal load injections and generation supplies. The remaining 18 bus bars were accommodated by counting from the beginning again (i.e. the loads and generation supplies of buses 54, 55, 56...71 were supplied to the grid from buses 1, 2, 3 ... 18).

The Square grid in Fig. 23, is a high meshed grid, used here to model a transmission grid with a high degree of network looping guaranteeing a continuous operation. Their degree is $d_i = 4$, except at edges where $d_i = 3$ and corners where $d_i = 2$. Just like there was no logical method of mapping nodes from Nigerian to Cayley tree network, the Nigerian network is also re-arranged into square grid using the same Nigerian bus identities (i.e. 1, 2, 3 ... 64) along the square-like topology and still maintaining their individual nodal load injections and generation supplies. The remaining 7 buses were accommodated by counting from the beginning again (i.e. the loads and generation supplies of buses 65, 66, 67...71 were injected into the grid from buses 1, 2, 3 ... 7). Table IV shows the identification (i.e. bus I.D.) of the Nigerian network buses (i.e. bus names) used in the serial mapping of the network into Cayley tree and Square power grids. It also shows their bus types and typical voltage magnitudes in per unit (p.u.) at undisturbed operations. The PV type of bus represents a generator bus while the PQ type of bus represents a load bus or any other network bus that is not a slack bus. In practice, a typical PV bus type supply load(s) too.

Appendix B
Single Line Diagrams and Topologies of the Simulated Networks

Here, the remaining single line diagrams and/ the topologies of the Square, Cayley-tree, Ghana and IEEE 118 test power grids are shown. They show the network components at their respective substations/buses.

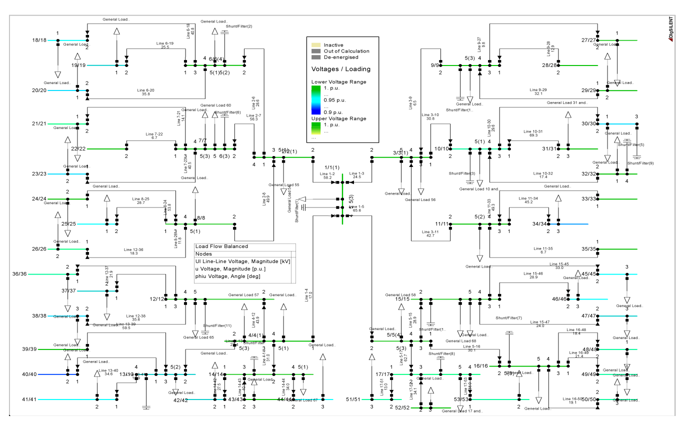

Fig. 21: Single-Line Diagram of the Cayley-Tree Power Transmission Network

TABLE IV: Nigerian Mapping Auxiliary Table

Bus I.D.	Bus Name	Bus Type	U, Magnitude (p.u.)
1	ADIABOR T.S	PQ	0.9768145
2	AES G.S	PV	0.995801099
3	AFAM IV-V	PV	0.996160781
4	AFAM VI	PV	0.993810306
5	AHODA T.S	PQ	0.994417824
6	AJA T.S.	PQ	0.962437374
7	AJAOKUTA T.S	PQ	1.000404859
8	AKANGBA T.S	PQ	0.965738268
9	ALADJA T.S	PQ	0.981657904
10	ALAGBON T.S.	PQ	0.955622694
11	ALAOJI G.S	PV	0.992988082
12	ALAOJI T.S	PQ	0.991616639
13	ALIADE UGWUAJI T.S	PQ	0.97045223
14	ASCO G.S	PV	1.000069028
15	AYEDE T.S.	PQ	0.988806947
16	AZURA IPP	PV	1.005160409
17	B'KEBBI T.S	PQ	0.968718742
18	BENIN NORTH T.S	PQ	1.002178155
19	BENIN T.S	PQ	1.005553823
20	CALABAR T.S	PQ	0.974134535
21	DAMATURU T.S	PQ	0.978194544
22	DELTA G.S	PV	1.007157009
23	EGBEMA	PQ	0.984506301
24	EGBIN G.S.	PV	0.99274419
25	ERUNKAN T.S	PQ	0.987508236
26	EYAEN T.S	PQ	1.001779043
27	GANMO T.S	PQ	1.000335918
28	GBARAIN G.S	PV	1.002777311
29	GERE G.S/NIPP	PV	1.001442666
30	GOMBE T.S	PQ	0.969731566
31	GWAG T.S	PQ	0.994594387
32	IBOM G.S	PV	0.986938746
33	IHOVBOR NIPP	PV	1.00794673
34	IKEJA WEST T.S.	PQ	0.988923463
35	IKORODU T.S	PQ	0.993735573
36	IKOT-ABASI T.S	PQ	0.9867305
37	IKOT-EKPENE T.S	PQ	0.9889763
38	JALINGO T.S	PQ	0.944374569
39	JEBBA G.S	PV	1.00280727
40	JEBBA T.S	PQ	1.001418824
41	JOS T.S	PQ	0.969601298
42	KADUNA T.S.	PQ	0.967007891
43	KAINJI G.S	PV	0.996910629
44	KAINJI T.S	PQ	0.996864242
45	KANO T.S	PQ	0.922968219
46	KATAMPE T.S.	PQ	0.99552233
47	LOKOJA T.S	PQ	0.998843366
48	MAIDUGURI T.S	PQ	0.966390429
49	MAKURDI T.S	PQ	0.972825196
50	N/HAVEN SOUTH T.S	PQ	0.981792961
51	N/HAVEN T.S 1	PQ	0.982078586
52	ODUKPANI G.S	PV	0.989171671
53	OKEARO T.S.	PQ	0.986235245
54	OKPAI P.S	PV	0.995317929
55	PAPALANTO	PV	0.998086718
56	OMOKU G.S	PV	0.991486468
57	OMO PH1/NIPP	PV	1.00185377
58	ONITSHA T.S.	PQ	0.991974152
59	OSOGBO T.S.	PQ	1.004899792
60	OWERRI T.S	PQ	0.985669354
61	Owerri 132KV	PQ	0.982770373
62	PARAS ENERGY G.S	PV	0.998483419
63	PH MAIN T.S	PQ	0.991720059
64	RIVERS IPP G.S	PV	0.992389412
65	SAKETE T.S.	PQ	0.945484451
66	SAPELE NIPP	PV	0.996008067
67	SAPELE G.S	PV	1.009414934
68	SHIRORO G.S	PV	0.997078769
69	TRANS-AMADI	PV	0.992027087
70	YOLA T.S	PQ	0.963147203
71	Yenagoa T.S	PQ	1.001950015

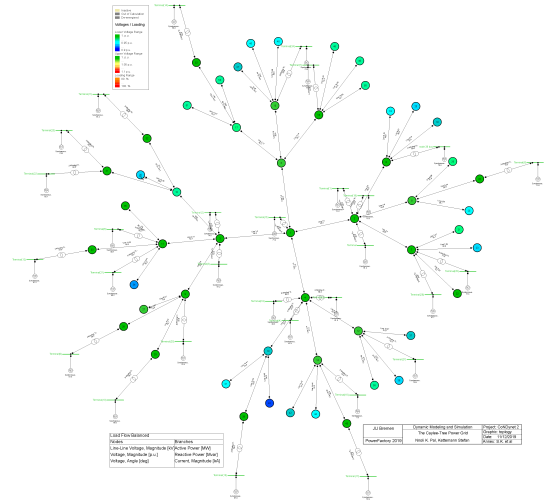

Fig. 22: The Topology of the Cayley-Tree Power Network

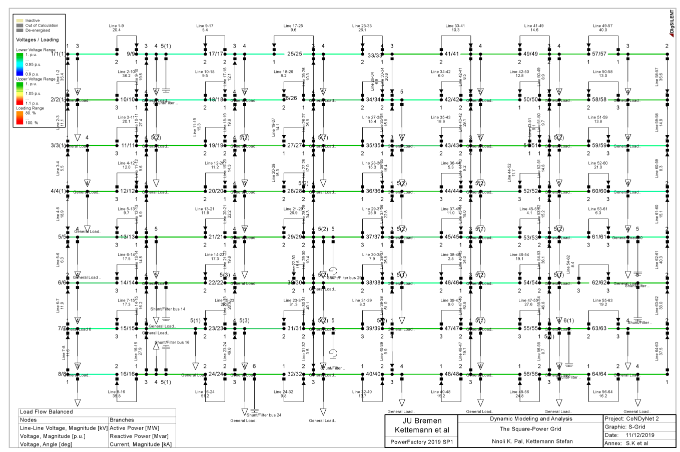

Fig. 23: Single-Line Diagram of the Square Power Transmission Network

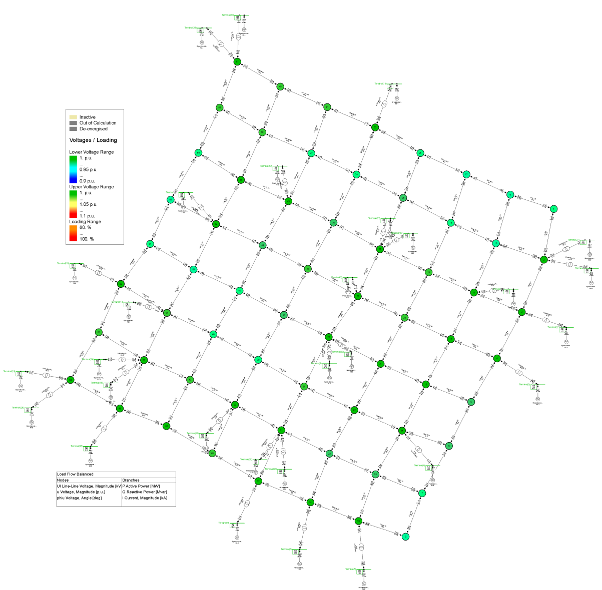

Fig. 24: The Topology of the Square-Power Network

APPENDIX C
VOLTAGE PROFILES OF THE POWER GRIDS

The voltage profiles of the Nigerian, Square, Cayley-tree, Ghana and IEEE 118 bus test power grids at steady state (i.e. normal operations) conditions are shown in the Figures 25, 26, 27, 28 and 29 respectively.

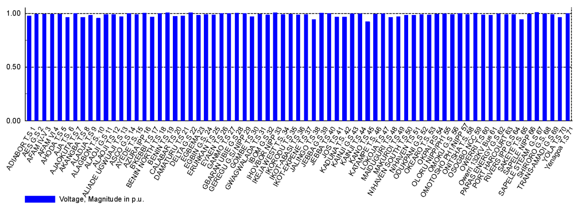

Fig. 25: Voltage Profile of Bus Bars: Nigerian Power Grid

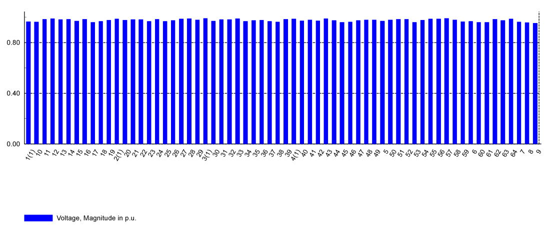

Fig. 26: Voltage Profile of Bus Bars: Square Power Grid

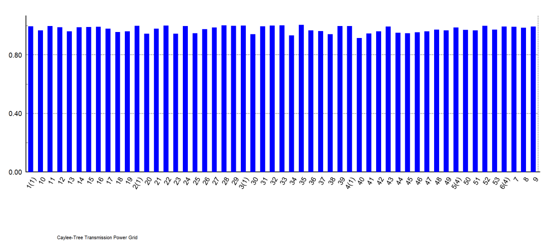

Fig. 27: Voltage Profile of Bus Bars: Cayley-Tree Power Grid

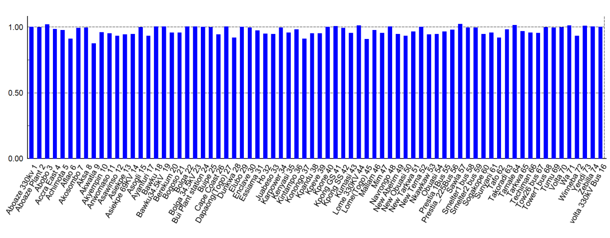

Fig. 28: Voltage Profile of Bus Bars: Ghana Power Grid

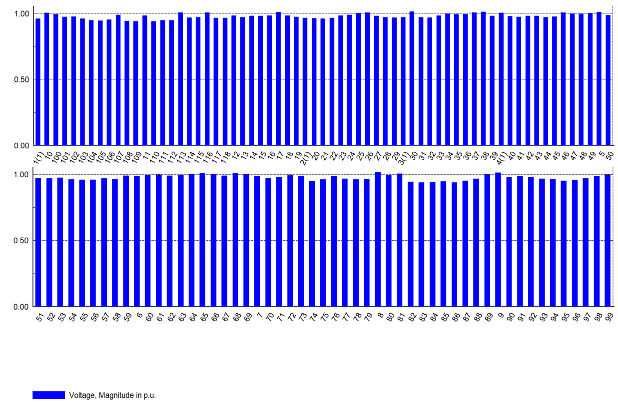

Fig. 29: Voltage Profile of Bus Bars: IEEE 118 Bus Test-Grid